

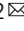


## Imaging and sensing of pH and chemical state with nuclear-spin-correlated cascade gamma rays via radioactive tracer

Kenji Shimazoe<sup>1</sup>, Mizuki Uenomachi<sup>2</sup> & Hiroyuki Takahashi<sup>3</sup>

Single-photon-emission computed tomography (SPECT) and positron-emission tomography (PET) are highly sensitive molecular detection and imaging techniques that generally measure accumulation of radio-labeled molecules by detecting gamma rays. Quantum sensing of local molecular environment via spin, such as nitrogen vacancy (NV) centers, has also been reported. Here, we describe quantum sensing and imaging using nuclear-spin time-space correlated cascade gamma-rays via a radioactive tracer. Indium-111 ( $^{111}\text{In}$ ) is widely used in SPECT to detect accumulation using a single gamma-ray photon. The time-space distribution of two successive cascade gamma-rays emitted from an  $^{111}\text{In}$  atom carries significant information on the chemical and physical state surrounding molecules with double photon coincidence detection. We propose and demonstrate quantum sensing capability of local micro-environment (pH and chelating molecule) in solution along with radioactive tracer accumulation imaging, by using multiple gamma-rays time-and-energy detection. Local molecular environment is extracted through electric quadrupole hyperfine interaction in the intermediate nuclear spin state by the explicit distribution of sub-MeV gamma rays. This work demonstrates a proof of concept, and further work is necessary to increase the sensitivity of the technique for in vivo imaging and to study the effect of scattered radiation for possible application in nuclear medicine.

<sup>1</sup>Department of Bioengineering, School of Engineering, The University of Tokyo, 7-3-1Hongo, Bunkyo-ku, Tokyo, Japan. <sup>2</sup>Department of Nuclear Engineering and Management, School of Engineering, The University of Tokyo, 7-3-1Hongo, Bunkyo-ku, Tokyo, Japan. <sup>3</sup>Institute of Engineering Innovation, School of Engineering, The University of Tokyo, Yayoi, Bunkyo-ku, Tokyo, Japan. ✉email: [shimazoe@bioeng.t.u-tokyo.ac.jp](mailto:shimazoe@bioeng.t.u-tokyo.ac.jp); [mizuki.uenomachi@riken.jp](mailto:mizuki.uenomachi@riken.jp)

Since the advent of nuclear-medicine imaging in the 1950s, single-photon-emission computed tomography (SPECT)<sup>1–4</sup> and positron-emission tomography (PET)<sup>5–7</sup> have become widely used clinical diagnosis and molecular imaging methods. In SPECT imaging, physical collimators with high-density materials are used to determine the direction of gamma rays emitted from single-photon emission nuclides. SPECT typically utilizes relatively low-energy single gamma rays (50–300 keV), and the locations of radio-labeled molecules are determined by the detection of these gamma rays. The accumulation level of radio-labeled molecules is evaluated and utilized for the diagnosis of several diseases, such as cancer, dementia, or Parkinson's, and evaluation of therapeutic nuclides. For example, diagnostic <sup>111</sup>In-ibritumomab tracers combined with therapeutic <sup>90</sup>Y (Zevalin) are used for tumor detection and therapy. Radioactive nuclides, such as <sup>111</sup>In, <sup>99m</sup>Tc, <sup>131</sup>I, and <sup>177</sup>Lu, are used for diagnostic and/or therapeutic purposes<sup>3,8–12</sup>. Nuclear medical imaging is generally characterized by its extremely high sensitivity ( $10^{-12}$  mol = pmol) towards sub-MeV gamma-rays compared with other molecular imaging modalities. On the other hand, there are recent reports of quantum sensing extracting the local molecular environment information, such as of nitrogen-vacancy (NV) centers<sup>13–15</sup>, which can obtain the information, such as electric field, magnetic field, and pH, via controlled spin states with high accuracy. However, NV centers are mostly applied to the phenomena at the cell level because of the utilization of visible photons in imaging. For medical diagnosis in humans, a quantum sensor with high-penetrating-power photons will be preferable to extract the information at an individual level. Here, we explore the use of gamma-ray emitting nuclides as quantum sensors via the nuclear spin state. SPECT imaging utilizes a single-photon emitted from gamma decay nuclei, as indicated by its name. However, among these radioactive SPECT nuclides, there are several special nuclides emitting more than two gamma-rays in a cascaded way with a short duration of intermediate states (Supplementary Figures 1a–1c). For example, <sup>111</sup>In emits two gamma-ray photons of 171 keV and 245 keV with 84.5 ns time constant after electron capture; <sup>177</sup>Lu emits 208 keV and 113 keV with approximately 0.5 ns time constant following beta minus decay<sup>16,17</sup>. These cascade gamma-rays have an angular correlation that originates from the nuclear spin state in its decay<sup>18</sup>. The angular distribution of gamma-ray emission  $W(\theta, t)$  is generally described using Legendre poly-nominal  $P_k$ , where  $k$  is the even constant determined from the conservation of angular momentum:

$$W(\theta, t) = \frac{1}{\tau_N} e^{-\frac{t}{\tau_N}} \left[ 1 + A_{22} P_2(\cos\theta) + \dots \right] = \frac{1}{\tau_N} e^{-\frac{t}{\tau_N}} \sum A_{kk} P_k(\cos\theta), \quad (1)$$

where  $P_2(\cos\theta) = \frac{3\cos^2\theta - 1}{2}$  and  $\tau_N$  is the mean lifetime of the intermediate nuclear state, which is  $1.22 \times 10^{-7}$  s for <sup>111</sup>In. If the direction of the first gamma-ray is chosen as the quantization axis, the second gamma-ray is said to have anisotropic emission to the first gamma-ray.  $A_{22}$  and  $A_{kk}$  are angular correlation coefficients. The highest term of this expansion is decided by the selection rule:  $k_{max} = \text{Min}(2I, 2I_1, 2I_2)$ . This gamma-ray emission polarization and its application to detect external field through the intermediate states is called perturbed angular correlation (PAC)<sup>19–21</sup>, which has been used in chemical analysis and nuclear physics research. In nuclear physics research, many nuclides are investigated to determine their characteristics, such as decay mode. In the 1970s, some studies revealed the correlation of the external field environment and its emission through electric quadrupole interaction via nuclear spin with one simple coincidence detector<sup>22,23</sup> and suggested possible biological applications;

however, there have been no studies on simultaneous imaging and quantum sensing of pH and other molecular environments.

In some previous studies, double photon emission computed tomography (DPECT<sup>24,25</sup>) imaging has been proposed for localizing the accumulation with higher signal to background ratio by taking the intersection of two back-projection lines via two cascade photons. DPECT imaging localizes the radioactive tracer position with a single coincidence event compared with conventional SPECT, which typically requires the rotation of detectors. However, these methods have only been used to detect the accumulation of radio-labeled molecules, and local molecular environment sensing was not investigated.

With multiple-dimension gamma-rays decay detection techniques combined with nuclear spin, we propose local environment quantum sensing, such as pH or chemical state, and its simultaneous imaging using cascade decay radioactive nuclide. We characterized the distribution of gamma-ray time-space distribution in several different local environments surrounding molecules by developed ring-shaped detectors and demonstrated the imaging capability of clinically available <sup>111</sup>In SPECT nuclear-medicine tracer together with pH and chelating molecule sensing. This simultaneous imaging and quantum sensing will provide nuclear-medicine diagnosis with local molecular environment sensing and a platform of quantum sensing in medical diagnosis with naturally polarized photons via nuclear spin. This work demonstrates a proof of concept, and further work is necessary to increase the sensitivity of the technique for in vivo imaging and to study the effect of scattered radiation for possible application in nuclear-medicine.

## Results

**Sensing pH with gamma-ray emission.** First, we evaluated the change of gamma-ray emission distribution caused by different pH values in <sup>111</sup>In solution. <sup>111</sup>Indium chloride solution (from Nihon-Medi Physics) with pH of 1.9 (measured with Horiba F-72M pH meter) is used as a standard sample. <sup>111</sup>In nuclide emits two cascade photons of 171 keV and 245 keV with a time constant of 84.5 ns after electron capture (EC) and emission of 22 keV X-ray (Fig. 1a). The initial state after EC has a nuclear spin of 9/2 (parity  $\pi = +$ ), intermediate state nuclear spin of 7/2 (parity  $\pi = +$ ), and a final state with nuclear spin of 1/2 (parity  $\pi = +$ ). The first decay mode is magnetic dipole M1 (mixed with electric quadrupole E2), and the second decay mode is E2. The detection of the first gamma photon corresponds to selecting nuclear spin state decaying with photon emission with  $m = 1$  or  $m = -1$  and intermediate spin state polarizes, which results in the anisotropic distribution of second gamma-rays in the quantization axis of the first gamma photon. The electric quadrupole interaction between nuclear spin in the intermediate state and local external environment (pH and molecular interaction) will result in the perturbed distribution of gamma photons (Fig. 1a) with sub-MeV energy. The arrival time, energy, and position are detected with a gamma-ray detector array with 512 channels with 8 detectors of  $8 \times 8$  arrays surrounding the target radioactive tracers (Fig. 2a). Within the determined time window ( $-50$  ns to  $+200$  ns) and energy window (171 keV and 245 keV  $\pm 10\%$ ), the angles between the two coincident correlated gamma photons are calculated and plotted (Fig. 2b, c). The plots are normalized by the data with the time window (less than minus 50 ns or more than plus 200 ns) and energy window (171 keV and 245 keV  $\pm 10\%$ ), which are assumed to be uncorrelated, random photons with the isotropic distribution. The normalization of correlated events by the uncorrelated events will work to eliminate the effect of geometry including the scattering in the target region.

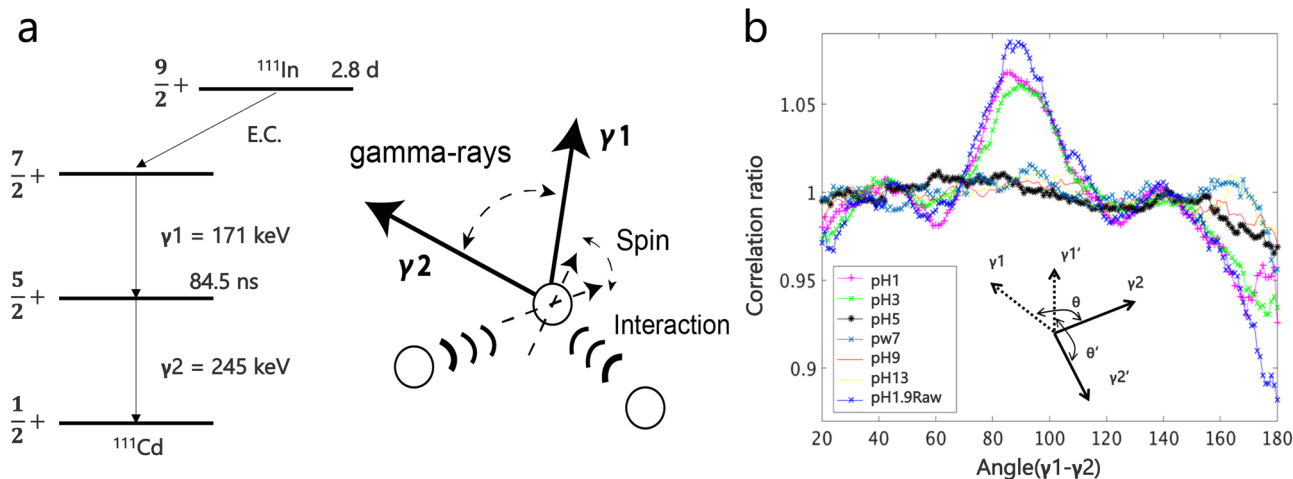


**Fig. 1**  $^{111}\text{In}$  decay scheme and pH sensing using gamma-ray photons and the measured angular correlations. **a**  $^{111}\text{In}$  nuclide decay emits two successive cascade photons with energy of 171 keV and 245 keV via nuclear spin state after electron capture. The half-life of  $^{111}\text{In}$  is approximately 2.8 days and it is widely used in nuclear medicine. Cascade decay of  $^{111}\text{In}$ , which has the initial nuclear spin  $7/2$  (parity  $\pi = +$ ), intermediate  $5/2$  (parity  $\pi = +$ ), and ground state  $1/2$  (parity  $\pi = +$ ). The intermediate state has a time constant of 84.5 ns. The hyperfine interaction between the intermediate spin state with the external electric gradient results in the angular change between two successive gamma-rays. The gamma-ray angular correlation can be an indicator of its local molecular environment. **b** The measured angular distribution with a single detection setup for different pH values. pH 1, pH 1.9, and pH 3 have significantly high correlation ratio along the  $90^\circ$  direction and a low correlation along  $180^\circ$ , which is approximately more than 5%. This is caused by nuclear spin selection with coincidence detection. This indicates the detection of two gamma-ray correlation, which provides the information of the local pH state surrounding the radiotracers.

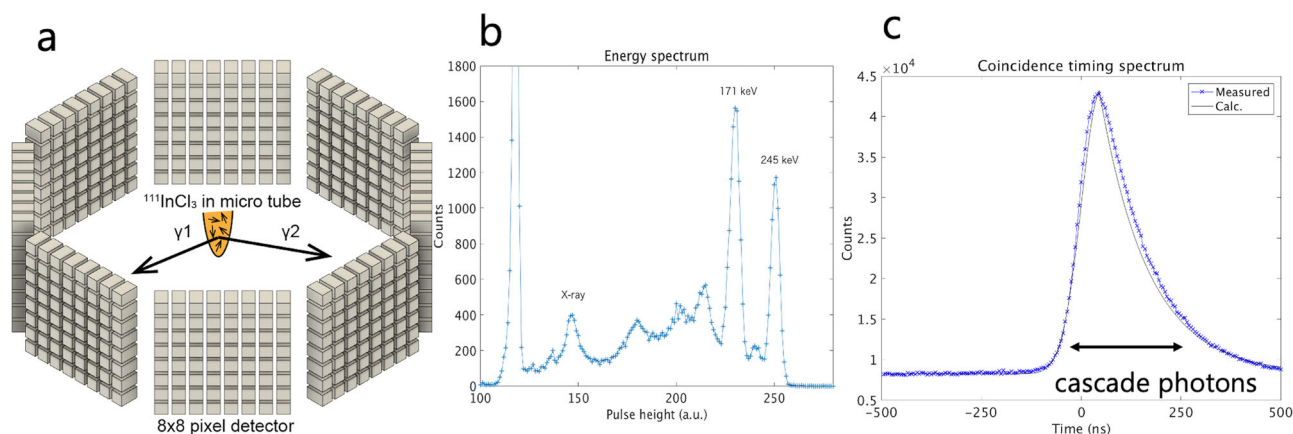


**Fig. 2** Detector geometry for measuring the angular correlation, measured energy, and timing spectra. **a** Gamma-ray detector geometry for measuring the angular correlation in cascade photons. **b** The measured energy spectrum of  $^{111}\text{In}$  shows clear separation of 171 keV and 245 keV gamma-ray photons. **c** The measured and calculated coincidence time difference spectrum. The angles are calculated with the coincidence events within the fixed time window.

Figure 1b shows the measurement data of gamma-ray angular distribution with seven different pH conditions, prepared by mixing  $^{111}\text{InCl}_3$  raw solution with NaOH, HCl, and phosphoric acid solutions (Supplementary Table 1). The graph shows the clear transition of gamma-ray emission distribution in  $^{111}\text{In}$ -containing solution from pH3 to pH5. No correlation is observed at pH larger than the transition around 3. In the raw solution (pH = 1.9), pH 1 and pH 3, the second gamma-ray emission has a significant increase of approximately  $90^\circ$  and decrease of approximately  $180^\circ$  in the quantization axis of the first gamma-ray in cascade decay. These results correspond to the manual theoretical calculation of polarization described in the Methods section (Supplementary Fig. 1b, 1c). The difference between calculation and measurement is caused by the effect of random coincidence events within the fixed time window and extra-nuclear interaction. The results indicate the feasibility of pH detection by gamma-ray emission distribution via nuclear spin

interaction with the local chemical environment. The radioactivity of solutions is approximately 0.8–1.2 MBq, which approximately corresponds to 0.46 pmol and 0.69 pmol. The gamma-ray emissions are measured for approximately 30 min, which is a standard measurement time range in clinical nuclear-medicine imaging.

**Change in gamma-ray emission with a chelating molecule.** Second, we have examined the response to the chelating molecule (Psyche-DOTA[ $^{111}\text{In}$ ]) trapping  $^{111}\text{In}$  atoms, which can be used to attach the labeled molecule to antibodies<sup>24</sup> in biological studies. The Cupid-Psyche system is a versatile diagnostic and therapeutic system for advanced cancer based on the strong noncovalent interaction of streptavidin and biotin. Psyche is a modified artificial biotin. Psyche-DOTA[ $^{111}\text{In}$ ] is designed for nuclear-medicine imaging combined with Cupid, which is a low immunogenic mutated streptavidin for pre-targeting therapy. The

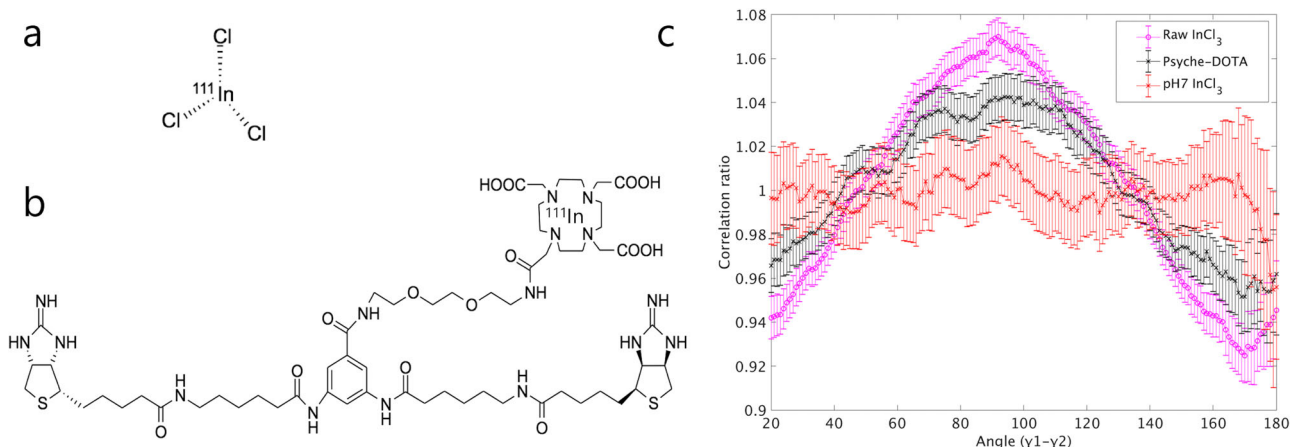


**Fig. 3** Gamma-ray correlation distribution of Psyche-DOTA[ $^{111}\text{In}$ ], raw  $^{111}\text{InCl}_3$ , and pH 7  $^{111}\text{InCl}_3$  solution. **a** Molecular structure of  $^{111}\text{InCl}_3$ . The raw  $^{111}\text{InCl}_3$  solution is provided by Medi-Physics for SPECT application in a solution with pH value of 1.9. Other samples with different pH are produced by mixing the raw solution with other solutions listed in supplementary table 1. **b** The chemical structure of Psyche conjugated with DOTA[ $^{111}\text{In}$ ].  $^{111}\text{In}$  radioactive atom is trapped in the chelating site of Psyche-DOTA by mixing and heating. **c** Correlation ratio depending on the angle from first gamma-ray photon to second gamma-ray photons in three different solutions, namely raw  $^{111}\text{InCl}_3$ , Psyche-DOTA[ $^{111}\text{In}$ ], and pH 7  $^{111}\text{InCl}_3$ . The error bars show  $\pm 1$  standard deviations. Clear difference (approximately 1, 1.04, and 1.06 in pH 7, Psyche-DOTA, and raw  $\text{InCl}_3$  (pH 1.9) in gamma-ray emission is observed, which indicates the detection possibility of chemical bond state in nuclear medical imaging.

Psyche-DOTA structure captures the  $^{111}\text{In}$  atom with four fingers of N atoms. Psyche-DOTA[ $^{111}\text{In}$ ] is prepared by mixing  $^{111}\text{InCl}_3$  solution and Psyche-DOTA with a molar concentration of 1:1000 and heating it to 80 °C for 15 min. In the actual measurement protocol of diagnosis, Psyche-DOTA is used by combining with alpha-CEA-Cupid for labeling the antibody. Psyche-DOTA[ $^{111}\text{In}$ ] has a measured pH value of 4.5. The chemical descriptions of  $^{111}\text{InCl}_3$  and Psyche-DOTA[ $^{111}\text{In}$ ] are shown in Fig. 3a, b. Figure 3c compares the results of three different conditions (raw (pH = 1.9), pH = 7 and Psyche-DOTA[ $^{111}\text{In}$ ]). The results for the pH of 1.9 and pH of 7 were consistent with the results of the previous experiment, and Psyche-DOTA showed a significant increase at 90 degree compared with the results for pH 7, which will be the most probable condition in the human body. This shows the feasibility of detecting the chelated and unchelated state of a radioisotope in solution through the gamma-ray correlation data. The detection of the chelation state of a radioisotope provides important information as to whether the radioisotope is captured in DOTA of the Psyche-Cupid system or not.

**Imaging and sensing pH with gamma-ray emission.** Third, for demonstrating the proof-of-concept imaging of accumulation with pH sensing, double photon imaging is performed with coincidence detection using four physically collimated gamma-ray detectors array. The four detectors have  $8 \times 8$  imaging voxels and are located in the 0, 90, 180, and 270° directions. The time, energy, and positions of all the gamma-ray photons are recorded. Timing selection (minus 50 ns to plus 200 ns) and energy selection (171 keV and 245 keV  $\pm 10\%$ ) are applied to extract the correlated gamma ray photons (Fig. 4a). Three different pH combination patterns (pH 1–pH 1, pH 1–pH 9, pH 3–pH 12) of two  $^{111}\text{InCl}_3$  sources with radioactivity of 2 ~ 3 MBq (1.15 pmol ~ 1.73 pmol) are used. The image of radioactive tracer accumulation was reconstructed with intersection extraction back-projection (Fig. 4a), which can localize the source position into one single point with coincidence gamma-ray detection. The parameter indicating the pH value is extracted by calculating the anisotropic parameter  $A_x$  of 90° and 180°, within the region of interest (ROI) in the reconstruction voxels. The size of ROI A and ROI B is set to

be  $6.4 \times 6.4 \times 6.4$  mm in the reconstructed image.

$$A_x = \frac{\sum_{t=-200 \text{ ns}}^{t=200 \text{ ns}} w_{12}(90^\circ, t) \times w_{34}(90^\circ, t) + w_{23}(90^\circ, t) \times w_{14}(90^\circ, t)}{\sum_{t=-50 \text{ ns}}^{t=50 \text{ ns}} w_{13}(180^\circ, t) \times w_{24}(180^\circ, t) \times 2}, \quad (2)$$

where  $w_{ii}$  indicates the measured counts of coincidence events between detector  $i$  and detector  $i$ , which is also shown in Fig. 4a. For reference and correction purposes, the parameter of random “chance” coincidence events  $A_{\text{random}}$  are calculated with a different integration time.

$$A_{\text{random}} = \frac{\sum_{t=-200 \text{ ns}}^{t=-50 \text{ ns}} w_{12}(90^\circ, t) \times w_{34}(90^\circ, t) + w_{23}(90^\circ, t) \times w_{14}(90^\circ, t)}{\sum_{t=-500 \text{ ns}}^{t=-50 \text{ ns}} w_{13}(180^\circ, t) \times w_{24}(180^\circ, t) \times 2}. \quad (3)$$

Figure 5a and b show the successfully reconstructed three-dimensional image of  $^{111}\text{In}$  radiotracer from the side and top views, and simultaneous pH imaging with different pH combinations. Two  $^{111}\text{InCl}_3$  solutions are clearly visualized and the pH condition is identified with the developed gamma-ray imaging system. The significant transition of the pH anisotropic parameter from pH 1.9–3 to pH 9–12 is also observed (Fig. 4b), which corresponds to the results shown in Fig. 1b. The noncorrelation data without photon coincidence detection is also shown. This proves the feasibility of simultaneous accumulation and local molecular environment imaging through  $^{111}\text{In}$  cascade nuclides via nuclear spin quadrupole interaction. The naturally polarized gamma-photons will provide the capability of local microenvironment quantum sensing with high sensitivity (pmol) by coincidence detection techniques. Supplementary Figure 3a presents the results of anisotropy with decreased counts, i.e., 1/3 and 1/10. A correlation is still observed in the 1/3 concentration, whereas the 1/10 concentration lost the correlation, indicating that a sensitivity higher by an order of 2–3 is required. The experiment was conducted both with and without water to observe the effect of scattering. Supplementary Figure 3b presents the results of anisotropy of the raw solution (~pH 1.9) in comparison to the uncorrelated random events. Both showed a

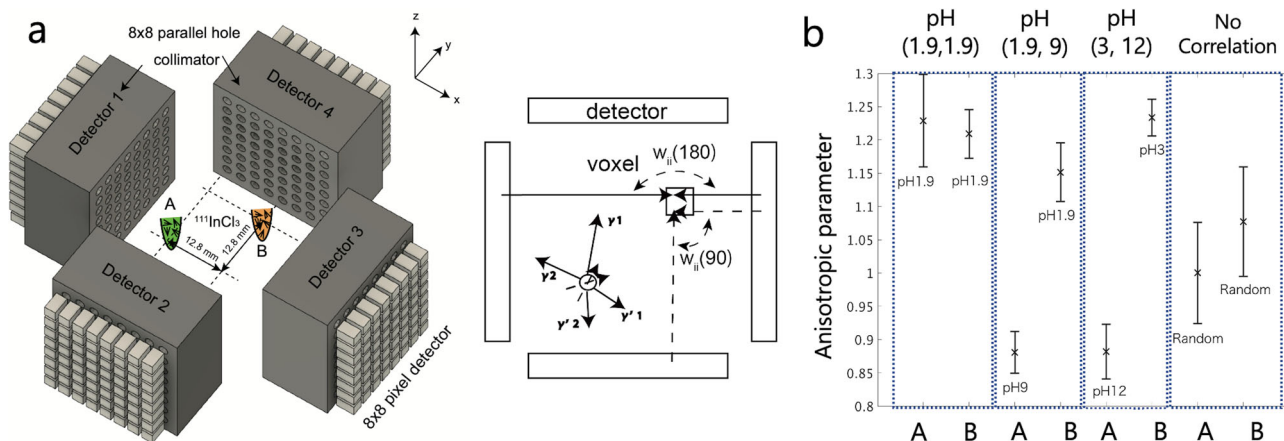


**Fig. 4 Experimental setup of imaging and sensing pH value.** **a** Gamma-ray detectors surround the target radiotracer to cover the  $2\pi$  direction. All the gamma-ray events are recorded with time, deposited energy, and their positions in the list-mode data. Angles are calculated from positions of coincidence events. Experimental setup to validate the simultaneous imaging and pH sensing with radiotracers. Three  $^{111}\text{In}$  solutions with different pH conditions in tube (A, B) of (pH 1.9, pH 1.9), (pH 9, pH 1.9), and (pH 12, pH 3) are used in the experiment. The gamma-ray photons are detected with four detectors equipped with parallel hole collimators. The images are reconstructed by identifying the intersected point with two coincidence photons. The anisotropic parameter is extracted by taking the ratio of  $90^\circ$  events and  $180^\circ$  events. **b** Anisotropic parameters calculated in each ROI A and B are plotted with error bars, where the error bars show  $\pm 2$  standard deviations. pH 1.9 and pH 3 groups have significant difference from pH 9 and pH 12 groups. Random indicates the noncoincidence events mimicking the isotropic emission. This verifies the capability of pH detection along with the imaging capability by the proposed method.

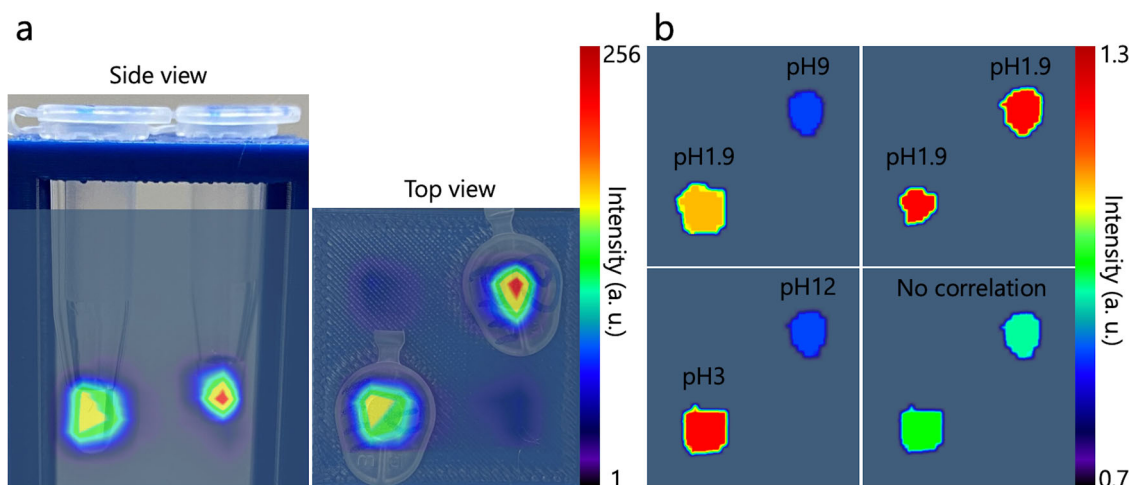


**Fig. 5 Simultaneous imaging and pH sensing of two  $^{111}\text{InCl}_3$  solutions with different pH conditions.** **a** Three-dimensional reconstructed image of the tracer accumulation with side view and top view ((A, B) = (pH 1.9, pH 9) case). The color indicates the intensity of radiotracer accumulation. Two  $^{111}\text{InCl}_3$  solutions in microtubes separated by 12.8 mm are successfully reconstructed by double photon imaging. The images are generated by registering the intersected coordinate of two coincidence back-projection lines (Fig. 4a). The reconstructed accumulation image with double photon method is overlaid on the optical image. Three combinations of (A, B) = (pH 1.9, pH 1.9), (pH 1.9, pH 9) and (pH 3, pH 12) are tested in the same geometric setup. **b** The four panels show the pH imaging results in three different combinations and noncorrelation case. The color indicates the value of the anisotropic parameters estimating pH value extracted by coincidence detection. The relation of pH and anisotropic parameters are shown in Fig. 4b. All the pH values are successfully estimated in three cases. Noncorrelation data are calculated from the noncoincidence data of measured gamma-rays.

similar value in this case, confirming the robustness of the method.

## Discussion

In this study, we quantified the effect of pH and a chelating molecule on  $^{111}\text{In}$  atoms used in commercial SPECT radioactive tracer. A significant transition from pH 3 to pH 5 was observed and considered to be caused by electric quadrupole interaction between the nuclear spin and external local field. Second, the gamma-ray photon emission from chelated  $^{111}\text{In}$  (PsychedOTA<sup>26</sup>) shows a significant difference from that of pH 7 controlled  $\text{InCl}_3$  solution. This shows the capability of determining

the chelation state of a radioisotope. Lastly, simultaneous imaging and pH sensing capability is demonstrated using the physical collimation method as a proof-of-concept study using a phantom. The double photon imaging method localizes the accumulation of  $\text{InCl}_3$  itself with high sensitivity, and anisotropic parameters of  $90^\circ/180^\circ$  ratio ( $A_x$ ) show the pH sensing capability within localized accumulation voxels. Since  $^{111}\text{In}$  is an already available radioactive SPECT tracer in clinical applications, the additional functionalities of detecting the microenvironment surrounding the radioisotope could be useful. However, the actual practical imaging method should be further optimized in terms of sensitivity and spatial resolution by choosing appropriate angular

resolving methods, such as multi-pinhole collimated imaging<sup>27</sup>, Compton imaging<sup>28–30</sup>, or coded aperture imaging. In particular, Compton imaging will be useful in the sub-MeV range to increase sensitivity. The feature of local environment sensing in combination with accumulation imaging can provide potential benefits to nuclear-medicine imaging with additional information to PET and SPECT technologies. In the application of biochemistry and biology, there are several molecules proposed for use in PAC measurements<sup>21–23</sup>. In addition, there are several possible candidate elements for radioactive tracers, such as <sup>181</sup>Hf, <sup>133</sup>Ba, and <sup>48</sup>Cr, with different energies and decay time constants that could provide different time-scale information of the local molecular environment<sup>31,32</sup>. The successful proof-of-concept imaging and detection of the difference between the chelated <sup>111</sup>In atom and the nonchelated one indicates the possibility of detection of molecular interaction and chemical bond state in the field of nuclear-medicine diagnosis when this method is used in combination with the appropriately designed molecules and nuclides. Especially this method can be considered as a quantum sensing and medical imaging method, which converts the hyperfine spin interaction in the energy range of  $\mu\text{eV}$  to the explicit gamma-ray photon with the energy of sub-MeV penetrating the human body to convey the information. This method can also be applied to measure other characteristics inside cells, such as viscosity, temperature, electric gradient, which are typically acquired by other quantum sensors, in the future research. We believe that this method of imaging and quantum sensing the local micro-environment in addition to its radio-labeled molecule accumulation will contribute to the nuclear medical imaging field.

## Methods

**Correlated gamma-ray emission via nuclear spin.** In cascade decay nuclides, such as <sup>111</sup>In, <sup>133</sup>Ba, <sup>60</sup>Co, and <sup>181</sup>Hf, there is a known property of angular correlation between two gamma rays in a successive manner<sup>33–36</sup>. Supplementary Figure 1a shows the general decay schemes in cascaded gamma-ray nuclides, which have the initial state ( $I_i, M_i$ ), intermediate state ( $I, M$ ), and final state ( $I_f, M_f$ ), and emit two gamma-rays of  $\gamma_1 : I_1, m_1$  and  $\gamma_2 : I_2, m_2$ , where  $I$  is nuclear spin,  $M$  is the nuclear spin magnetic quantum number,  $l$  is angular momentum, and  $m$  is the magnetic quantum number of gamma-ray photons. The total gamma-ray emission is isotropic; however, when the detection of the first gamma ray corresponds to the selection of quantum axis, the nuclear spin of the intermediate state polarizes and results in the anisotropic emission of the second gamma ray with respect to the first gamma ray. Supplementary Figure 1b shows the anisotropic emission of the second gamma ray to the first gamma ray, where the first gamma ray is assumed to be emitted and detected along  $0^\circ$ . The integrated emission intensity  $W(\theta)$  with no perturbation is expressed in the following equation:

$$W(\theta) = \sum_{M_f} \sum_{l_2} \sum_{m_2} \sum_M | \langle I, M; l_2, m_2 | I_i, M_i \rangle |^2 \cdot P(M) \cdot F_l^{m_2}(\theta), \quad (4)$$

where  $P(M)$  is the probability of the intermediate state expressed by

$$P(M) = \sum_{M_i} \sum_{l_1} \sum_{m_1} | \langle I_i, M_i; l_1, m_1 | I, M \rangle |^2 P_i(M_i), \quad (5)$$

and  $F_l^{m_2}(\theta)$  is the spherical harmonics function used to describe the emission direction.

The calculated anisotropic distribution with the Clebsch–Gordan coefficients in the case of the <sup>111</sup>In nucleus is shown in Supplementary Figure 1c using a line. The results simulated with Monte Carlo code (Geant4 by CERN<sup>37</sup>) are also plotted in the same figure with circle dots, with the same detector configuration shown in Fig. 2a. Both show an anisotropic response of more than 10% at an angle of  $90^\circ$  between two correlated gamma-ray photons.

If the nucleus is located in some specific external field, due to the interaction of the nucleus with an extranuclear field (hyperfine interaction), the change in angular correlation is observed by perturbed angular correlation (PAC). The change is mainly caused by nuclear quadrupole interaction with an electric field gradient. This results in changing the probability of the nucleus in the  $m_s$  state at a specific time, which was in  $m_i$  state at time 0. This is described as follows:

$$\langle m_s | \Lambda(t) | m_i \rangle = \sum_n \langle n | m_s \rangle \times e^{-iE_n t/\hbar} \langle n | m_i \rangle, \quad (6)$$

where  $\Lambda(t)$  is the time evolution operator,  $E_n$  is the eigenvalues, and  $\langle n |$  denotes the eigenvectors of the Hamiltonian. This will result in the perturbation of angular correlation of emitted gamma-ray photons.

**Sample preparation.** <sup>111</sup>Indium chloride (<sup>111</sup>InCl<sub>3</sub> Nihon Medi-Physics) is used as a standard solution. In the pH measurement experiment, pH is adjusted by mixing <sup>111</sup>InCl<sub>3</sub> with NaOH, HCl, and buffers that contain phosphoric buffer (PB) to achieve the desired pH value. The pH, radioactivity, and constituents of the used solutions are listed in Supplementary Table 1. The activity ranges from around 0.6 MBq to 1.2 MBq as verified with a dose calibrator (Capintec CRC-55tR). pH values are measured using a pH meter (Horiba F-72M pH meter). The solutions are prepared as small volumes of approximately 100  $\mu\text{L}$ , and the volume itself is negligible from the angular resolution of the used detection system. The samples are located in an air-conditioned room at a temperature of approximately  $20^\circ\text{C}$ . The <sup>111</sup>InCl<sub>3</sub> solution has a half lifetime of approximately 2.8 days, which is suitable for clinical use in diagnosis.

In the Psyche-DOTA experiment, Psyche-DOTA is mixed with <sup>111</sup>InCl<sub>3</sub> raw solution at a concentration of 1:1000 and incubated at approximately  $80^\circ\text{C}$  to trap the <sup>111</sup>In atoms in the binding site. The labeling rate of Psyche-DOTA is approximately 80%.

**Detectors.** For detecting the time, space, and energy data of emitted gamma-ray photons from the sample solutions, a high-resolution Ce:Gd<sub>3</sub>Al<sub>2</sub>Ga<sub>3</sub>O<sub>12</sub> (HR-GAGG) scintillator<sup>38</sup> was used as a conversion material from gamma rays to optical photons (wavelength  $\sim 520\text{ nm}$ ). A HR-GAGG scintillator has the characteristics of desirable energy resolution (4% with an avalanche photodiode sensor), high light yield (56,000 photons/MeV), high density (6.63 g/cm<sup>3</sup>), moderate timing resolution (150 ns), nondeliquescence, and nonself-irradiation for our experiment. Scintillators consisting of  $8 \times 8$  HR-GAGG arrays of  $2.5 \times 2.5 \times 4.0$  (thickness) mm were used to detect the photo-absorption events of gamma rays emitted from the <sup>111</sup>In nucleus in one module. The pitch size was 3.2 mm, and each crystal was separated by BaSO<sub>4</sub> reflectors of 700- $\mu\text{m}$  thickness. Each GAGG array was coupled to an  $8 \times 8$  array of SiPMs (Hamamatsu MPPC S13361-3050) and was then wrapped with Teflon tape. SiPMs convert the optical photons to corresponding electric signals, and the charge signals are transmitted to the following readout circuit that is described in the next section. One detector module has 64 channels of charge outputs.

In the pH and chelating molecule characterization experiment, eight detector modules are used to surround the measurement target solution for covering the solid angle to characterize the relation between microenvironment and gamma-ray emissions. One detector pixel approximately corresponds to  $5.6^\circ$ , because one ring has 64 channels in  $360^\circ$ . The vertical coverage is approximately  $45^\circ$ , and the limitation of coverage requires detector geometry calibration in the analysis. The diameter of a gamma-ray detector ring is adjusted to be 69 mm, and eight modules are located to form an octagon (Fig. 2a). Figure 2b and c show the measured energy spectrum and coincidence time spectrum in a single measurement. The energy spectrum shows a clear peak of two cascade gamma-ray photons having energies of 171 keV and 245 keV in addition to some X-ray events and Compton scattered events; further,  $\pm 10\%$  of these energies are used in the coincidence detection. In the timing spectrum, the dotted line shows the measured decay time of 84.5 ns originating from the intermediate state of the nuclear spin. The calculated plot of a Gaussian distribution convoluted with an exponential decay function is also shown as a reference.

In the imaging experiment, four modules with physical collimations are used to surround the two <sup>111</sup>InCl<sub>3</sub> solutions for detecting the double photons emitted from the radioisotope simultaneously. Physical collimations are made of Pb (Lead) with 15-mm thickness to limit the direction of incoming gamma rays to the pixel detectors. Each collimator has  $8 \times 8$  parallel holes (2-mm diameter, 3.2-mm pitch) individually coupled to the pixels in the detectors.

**Signal processing and data acquisition.** The charge signals from the HR-GAGG coupled to SiPMs were processed using parallel, dynamic, time-over-threshold (dToT)<sup>39,40</sup> signal processing circuits. The dToT method offers low power consumption and multi-channel parallel signal processing compared with conventional pulse-height measurements with analog-to-digital converters (ADCs) (Supplementary Figure 2). The dToT signal processing circuit consists of an amplifier, a dynamic-threshold generator, and a comparator with feedback dynamic-threshold generator with two monostable multi-vibrators. It provides digital signals with a proportional pulse width and its rising edge represents the gamma-ray incident time. The intrinsic time resolution is approximately 50 ns (full-width-half-maximum; FWHM), which will be enough for integrated angular correlation measurement, although it could be improved in future experiments. As shown in Fig. 2c, the coincidence timing spectrum is correctly acquired using all the channels.

The ToT digital outputs from gamma-ray detectors are transferred to field-programmable gate array (FPGA, Xilinx Kinetex7 XC7k70T) data-acquisition (DAQ) systems through KEL coaxial cables. The time stamp, position channel number, and ToT pulse width corresponding to the energy are recorded in the list mode in a solid-state drive (SSD) with 2.5 ns / 1 ns accuracy in parallel. In the pH experiment, the information from all the 512 channels is recorded in the binary data format. In the imaging experiment, 256 channels are used. Multiple DAQs are synchronized with external clocks with a frequency of 1 kHz generated by a function generator. Time stamps are corrected from external clocks during offline analysis, which is important in the coincidence detection of two correlated gamma-ray photons.

**Data analysis and parameter extraction.** From the recorded binary data, coincidence events with energies of 171 keV and 245 keV  $\pm 10\%$  within a fixed time window of  $-500$  ns to  $+500$  ns are extracted for further analysis. Since each detector pixel has different gain characteristics, the peak positions are calibrated from the measured data. The events within the time window of  $-50$  ns to  $+200$  ns are regarded as true coincidence events with correlated gamma-ray photons. The events within the time window of  $-500$  ns to  $-200$  ns are regarded as random coincidence events with uncorrelated gamma-ray photons, which are used for calibration of the geometry effect in the system. After extraction of coincidence events, the angles from the first gamma ray (171 keV) and the second gamma ray (245 keV) are calculated from the dot product of two vectors corresponding to the cascade gamma rays. For correcting the geometry effect, random coincidence events (noncorrelation) are used. This is possible when there are enough random coincidence events, which are assumed to be noncorrelated photons. There is a significant increase in the counts, which is more than 5% in the peak along  $90^\circ$  and a decrease in counts along  $0^\circ$  and  $180^\circ$  for pH values less than 4. The chelation of  $^{111}\text{In}$  by Psyche-DOTA also shows the same trend in the angular distribution. These anisotropic emissions of cascade gamma rays are explained by the nuclear quadrupole interaction of an intermediate state with an external electric gradient field; however, further accurate investigation and control should be considered for future work.

**Imaging experiment, image reconstruction, and pH sensing.** The DPECT double photon imaging method is used in the image reconstruction<sup>41</sup>. The double photon imaging method uses the back-projection method with two coincidence events of 171 keV and 245 keV in the  $^{111}\text{In}$  case (Fig. 4a). One collimated event corresponds to one back-projection line in the reconstruction voxels, which is the same in the SPECT image reconstruction. The intersection points of two back-projection lines are extracted and recorded in the reconstruction voxels, which drastically reduce the signal to background ratio by eliminating the artifact caused by the single line. One of the advantages of this method is that there is no need to rotate the detector modules to acquire all the projection angles. The original detector position has  $8 \times 8 \times 8$  image voxels with dimensions of  $25.6 \times 25.6 \times 25.6$  mm<sup>3</sup>. The image was interpolated into  $29 \times 29 \times 29$  image voxels and converted into the DICOM format to visualize in the DICOM viewer. Four parallel hole collimated detector modules (1, 2, 3, and 4) are located to cover the angles of  $0^\circ$ ,  $90^\circ$ ,  $180^\circ$ , and  $270^\circ$ . From the results of image reconstruction, two  $^{111}\text{InCl}_3$  sources are clearly visualized (Fig. 5a). Two regions of interest (ROI) A and B are defined for extracting the anisotropic parameters ( $A_x$ ). Each ROI has a voxel size of  $25.6 \times 25.6 \times 25.6$  mm<sup>3</sup>, and coincidence events within the ROI were used for the calculation of the parameters.  $A_x$  values are calculated by taking the coincidence counts between several combinations of detector modules, as shown in the equation. The  $A_x$  data showed significantly lower values of less than 0.9 in pH 9 and pH 12 compared with that of more than 1.05 in pH 1.9 and pH 3 as plotted in Fig. 4b, where the error bars show  $\pm 2$  standard deviations. The results are consistent with those obtained from nonimaging, including the random coincidence data, which are located in approximately 1. By combining the extracted anisotropic parameters with imaging data, the pH quantum sensing and imaging is successfully demonstrated (Fig. 5b).

**Methodological improvement.** While we have demonstrated the feasibility of simultaneous imaging of  $^{111}\text{In}$  accumulation and detection of local molecular environments such as pH and the chemical bond state, there will be scope for improvement towards practical clinical applications. In the nonimaging experiment, the measurement time is approximately 30 min for detecting a level of pmol; however, in the imaging experiment, 480 min are required to locate the position and extract the parameters for the same level. The measured data shows the transition around pH5 and the typical value of pH in the body is approximately pH 6.5 to 7.5. It would be difficult to use direct pH detection and requires further investigation. Another possible way is the combination of other techniques, such as using liposomes, to enable controlled delivery<sup>42,43</sup>. The limitation in sensitivity could be caused by the collimation method, while determining the direction of incoming gamma rays. Double photon detection decreases the efficiency significantly as described in the multi-nuclide imaging demonstration<sup>44</sup>. Although we used double photon imaging to visualize the accumulation because of the capability of accumulation determination in one point, the rotating method with the same configuration could be investigated in the future. The use of active collimators is also proposed in a study<sup>45</sup> for increasing sensitivity. A multi-pinhole collimation method with higher sensitivity<sup>46</sup> or the Compton imaging<sup>47,48</sup> technique could be investigated in a future study to achieve higher sensitivity for sub-MeV gamma rays. An optimized collimation design in a DPECT system or further system design consideration will be necessary to increase the sensitivity for practical nuclear medical imaging (50 – 100 kBq/mL in organs). Recently, a research group also showed the improvement of detection efficiency in two orders using both pin-hole collimator and slit collimator in coincidence imaging<sup>49</sup>. In practical applications, the consideration of scatter effect is important as shown in the state-of-the-art SPECT imaging, and further development will be necessary to address this issue, which includes the scatter correction method. In terms of cascade gamma-ray nuclides, there are several candidates, such as  $^{181}\text{Hf}$ ,  $^{177}\text{Lu}$ , and  $^{48}\text{Cr}$ , which have

appropriate half-lifetimes in clinical use and moderate lifetimes of intermediate nuclear state for detecting an external field in biological applications. Furthermore, molecular design enclosing  $^{111}\text{In}$  or combination with nuclear dynamic polarization<sup>50</sup> will provide opportunities to monitor the state of trapping combined with correlated gamma-ray emission detection through the nuclear spin.

### Data availability

The data that support the findings of this study are available from the corresponding author upon reasonable request.

### Code availability

The codes that support the analysis of this study are available from the corresponding author upon reasonable request.

Received: 7 April 2021; Accepted: 24 December 2021;

Published online: 14 January 2022

### References

- Todd, R. W., Nightingale, J. M. & Everett, D. B. A proposed  $\gamma$  camera. *Nature* **251**, 132–134 (1974).
- Robu, S. et al. Preclinical evaluation and first patient application of  $^{99m}\text{Tc}$ -PSMA-I&S for SPECT imaging and radioguided surgery in prostate cancer. *J. Nucl. Med.* **58**, 235–242 (2017).
- Avram, A. M. Radioiodine scintigraphy with SPECT/CT: an important diagnostic tool for thyroid cancer staging and risk stratification. *J. Nucl. Med.* **53**, 754–764 (2012).
- Knoll, G. F. Single-photon emission computed tomography. *Proc. IEEE* **71**, 320–329 (1983).
- Brownell, G. L. Theory of radioisotope scanning. *Int. J. Appl. Radiat. Isot.* **3**, 181–192 (1958).
- Ter-Pogossian, M. M. et al. A positron-emission transaxial tomograph for nuclear Imaging (PETT). *Radiology* **89–98**, 114.1 (1975).
- Cherry, S. R. et al. Total-body PET: maximizing sensitivity to create new opportunities for clinical research and patient care. *J. Nucl. Med.* **59**, 3–12 (2018).
- Iagaru, A., Gambhir, S. S. & Goris, M. L.  $^{90}\text{Y}$ -ibritumomab therapy in refractory non-Hodgkin's lymphoma: observations from  $^{111}\text{In}$ -ibritumomab pretreatment imaging. *J. Nucl. Med.* **49**, 1809–1812 (2008).
- Delpassand, Ebrahim, S. et al. Safety and efficacy of radionuclide therapy with high-activity In-111 pentetreotide in patients with progressive neuroendocrine tumors. *Cancer* **23**, 292–300 (2008).
- Iskandrian, A. E. et al. Validation of left ventricular volume measurements by gated SPECT  $^{99m}\text{Tc}$ -labeled sestamibi imaging. *J. Nucl. Cardiol.* **5**, 574–578 (1998).
- Beauregard, J.-M., Hofman, M. S., Pereira, J. M., Eu, P. & Hicks, R. J. Quantitative  $^{177}\text{Lu}$  SPECT (QSPECT) imaging using a commercially available SPECT/CT system. *Cancer Imaging* **11**, 56–66 (2011).
- Sarkar, S. D., Kalappambath, T. P. & Palestro, C. J. Comparison of  $^{123}\text{I}$  and  $^{131}\text{I}$  for whole-body imaging in thyroid cancer. *J. Nucl. Med.* **43**, 632–634 (2002).
- Manson, N. B., Harrison, J. P. & Sellars, M. J. Nitrogen-vacancy center in diamond: Model of the electronic structure and associated dynamics. *Phys. Rev. B* **74**, 104303 (2006).
- Felton, S. et al. Hyperfine interaction in the ground state of the negatively charged nitrogen vacancy center in diamond. *Phys. Rev. B* **79**, 075203 (2009).
- Fujiwara, M. et al. Monitoring spin coherence of single nitrogen-vacancy centers in nanodiamonds during pH changes in aqueous buffer solutions. *RSC Adv* **9**, 12606–12614 (2019).
- Falk, F., Linnfors, A. & Thun, J. E. A search for after-effects of the  $^{111}\text{In}$  EC decay on the  $^{111}\text{Cd}$   $\gamma\gamma$  correlation. *Nucl. Phys. A* **152**, 305–316 (1970).
- Dias, M. S., Silva, F. F. & Koskinas, M. F. Standardization and measurement of gamma-ray probability per decay of  $^{177}\text{Lu}$ . *Appl. Radiat. Isot.* **68**, 1349–1353 (2010).
- Steffen, R. M. & Frauenfelder, H. Alpha, beta, and gamma-ray spectroscopy (ed. Siegbahn, K.) Chapter 19 997 (Amsterdam: North-Holland, 1968).
- Gwilliam, R., Sealy, B. J. & Vianden, R. The electrical and radioactive assessment of the transmutation doping of GaAs following implantation by  $^{111}\text{In}$ . *Nucl. Instrum. Methods Phys. Res. B* **63**, 106–108 (1992).
- Hesslink, W. H. A. et al. Band structure and hole-core coupling in  $^{111}\text{In}$ . *Nucl. Phys. A* **299**, 60–76 (1978).
- Pandian, S., Mathias, C. J. & Welch, M. J. Perturbed angular correlation studies of  $^{111}\text{In}$ -labelled platelets. *Int. J. Appl. Radiat. Isot.* **33**, 33–37 (1982).
- Goodwin, D. A., Goode, R., Brown, L. & Imbornone, C. J.  $^{111}\text{In}$ -labeled transferrin for the detection of tumors. *Radiology* **100**, 175–179 (1971).

23. Meares, C. F. & Westmoreland, D. G. The study of biological macromolecules using perturbed angular correlations of gamma radiation. *Cold Spring Harb. Symp. Quant. Biol.* **36**, 511–516 (1966).
24. Yoshihara, Y., Shimazoe, K., Mizumachi, Y. & Takahashi, H. Evaluation of double photon coincidence Compton imaging method with GEANT4 simulation. *Nucl. Instrum. Methods Phys. Res. A* **873**, 51–55 (2017).
25. Shimazoe, K. et al. Double Photon Emission Coincidence Imaging using GAGG-SiPM pixel detectors. *J. Inst.* **12**, C12055 (2017).
26. Sugiyama, A. et al. Cupid and Psyche system for the diagnosis and treatment of advanced cancer. *Proc. Jpn Acad. B* **95**, 602–611 (2019).
27. van Oosterom, M. N. et al. U-SPECT-BioFluo: an integrated radionuclide, bioluminescence, and fluorescence imaging platform. *EJNMMI Res* **4**, 56 (2014).
28. Sakai, M. et al. In vivo simultaneous imaging with  $^{99m}\text{Tc}$  and  $^{18}\text{F}$  using a Compton camera. *Phys. Med. Biol.* **63**, 205006 (2018).
29. Kishimoto, A. et al. First demonstration of multi-color 3-D in vivo imaging using ultra-compact Compton camera. *Sci. Rep.* **7**, 2110 (2017).
30. Krimmer, J. et al. Development of a Compton camera for medical applications based on silicon strip and scintillation detectors. *Nucl. Instrum. Methods Phys. Res. A* **787**, 98–101 (2015).
31. Wodniecki, P., Wodniecka, B., Kulinska, A., Uhrmacher, M. & Lieb, K. P. Hf and Zr aluminides with Bf-type structure studied by PAC with  $^{181}\text{Ta}$  and  $^{111}\text{Cd}$  probes. *J. Alloys Compd.* **351**, 1–6 (2003).
32. Raether, F. & Lieb, K. P. Magnetic moment of the 308 keV state in 48 V. *Hyperfine Interact* **34**, 61–64 (1987).
33. Hamilton, D. R. On directional correlation of successive quanta. *Phys. Rev.* **58**, 122–131 (1940).
34. Brady, E. L. & Deutsch, M. Angular correlation of successive gamma-ray quanta. *Phys. Rev.* **72**, 870–871 (1947).
35. Goertzel, G. Angular correlation of gamma-rays. *Phys. Rev.* **70**, 897–909 (1946).
36. Hemmingsen, L., Sas, K. N. & Danielsen, E. Biological applications of perturbed angular correlations of  $\gamma$ -ray spectroscopy. *Chem. Rev.* **104**, 4027–4062 (2004).
37. Agostinelli, S. et al. GEANT4—a simulation toolkit. *Nucl. Instrum. Methods Phys. Res. A* **506**, 250–303 (2003).
38. Kamada, K. et al. Cz grown 2-in. size Ce:Gd $_{3}$ (Al,Ga) $_{5}$ O $_{12}$  single crystal; relationship between Al, Ga site occupancy and scintillation properties. *Opt. Mater.* **36**, 1942–1945 (2014).
39. Shimazoe, K. et al. Dynamic time over threshold method. *IEEE Trans. Nucl. Sci.* **59**, 3213–3217 (2012).
40. Orita, T., Shimazoe, K. & Takahashi, H. The dynamic time-over-threshold method for multi-channel APD based gamma-ray detectors. *Nucl. Instrum. Methods Phys. Res. A* **775**, 154–161 (2015).
41. Uenomachi, M., et al. Double photon emission coincidence imaging with GAGG-SiPM Compton camera. *Nucl. Instrum. Methods Phys. Res. A* **954** (2020).
42. van der Geest, T., Laverman, P., Metselaar, J. M., Storm, G. & Boerman, O. C. Radionuclide imaging of liposomal drug delivery. *Expert Opin. Drug Deliv* **13**, 1231–1242 (2016).
43. Goel, S. et al. Positron emission tomography and nanotechnology: A dynamic duo for cancer theranostics. *Adv. Drug Deliv. Rev.* **113**, 157–176 (2017).
44. Uenomachi et al. Simultaneous multi-nuclide imaging via double-photon coincidence method with parallel hole collimators. *Sci. Rep.* **11**, 13330 (2021).
45. Omata, A. et al. Performance demonstration of a hybrid Compton camera with an active pinhole for wide-band X-ray and gamma-ray imaging. *Sci. Rep.* **10**, 1–9 (2020).
46. Ivashchenko, O., van der Have, F., Goorden, M. C., Ramakers, R. M. & Beekman, F. J. Ultra-high-sensitivity submillimeter mouse SPECT. *J. Nucl. Med.* **56**, 470–475 (2015).
47. Shimazoe, K. et al. Development of simultaneous PET and Compton imaging using GAGG-SiPM based pixel detectors. *Nucl. Instrum. Methods Phys. Res. A* **954** (2020).
48. Uenomachi, M. et al. Simultaneous in vivo imaging with PET and SPECT tracers using a Compton-PET hybrid camera. *Sci. Rep.* **11**, 17933 (2021).
49. Liu, X. et al. A 3-dimensional stationary cascade gamma-ray coincidence imager. *Phys. Med. Biol.* **66**, 225001 (2021).
50. Hu, K.-N. et al. Dynamic nuclear polarization with biradicals. *J. Am. Chem. Soc.* **126**, 10844–10845 (2004).

## Acknowledgements

This work was supported by the JST-PRESTO (Grant Number JPMJPR17G5) project, titled “Development Multi-Photon Time Space Correlated Imaging”. The authors wish to thank the organization for their financial support. The basic performance experiments were carried out under the support of Isotope Science Center, The University of Tokyo. The pH control and Psyche-DOTA chelating was conducted with the contribution of Assistant Prof. Sugiyama, Mr. Sensui, Mr. Ueki, and Mr. Ogane, and the authors would like to thank them for their support in the experiment. The authors are also grateful to Dr. Kushihiro for the preparation of the pH samples. The authors would like to thank Associate Prof. Kamada in Tohoku University for the material preparation of gamma-ray detectors and for the fruitful discussion with Associate Prof. Tomita in Nagoya University.

## Author contributions

The sensing concept and imaging experiments were conceived by KS and MU. The experiments were conducted by MU and analysis of all data was conducted by KS and MU. MU, KS, and HT contributed developing the system and discussing the results.

## Competing interests

The authors declare no competing interests.

## Additional information

**Supplementary information** The online version contains supplementary material available at <https://doi.org/10.1038/s42005-022-00801-w>.

**Correspondence** and requests for materials should be addressed to Kenji Shimazoe or Mizuki Uenomachi.

**Peer review information** *Communications Physics* thanks Richard Laforest and the other, anonymous, reviewer(s) for their contribution to the peer review of this work. Peer reviewer reports are available.

**Reprints and permission information** is available at <http://www.nature.com/reprints>

**Publisher's note** Springer Nature remains neutral with regard to jurisdictional claims in published maps and institutional affiliations.



**Open Access** This article is licensed under a Creative Commons Attribution 4.0 International License, which permits use, sharing, adaptation, distribution and reproduction in any medium or format, as long as you give appropriate credit to the original author(s) and the source, provide a link to the Creative Commons license, and indicate if changes were made. The images or other third party material in this article are included in the article's Creative Commons license, unless indicated otherwise in a credit line to the material. If material is not included in the article's Creative Commons license and your intended use is not permitted by statutory regulation or exceeds the permitted use, you will need to obtain permission directly from the copyright holder. To view a copy of this license, visit <http://creativecommons.org/licenses/by/4.0/>.

© The Author(s) 2022